Ce^{3+}/Tb^{3+} activated GdF_3, $KGdF_4$, and CeF_3 submicro/nanocrystals: Synthesis, phase evolution, and optical properties

Chunyan Cao
Department of Physics, Pukyong National University, Busan 608-737, Korea; and College of Mathematics and Physics, Jinggangshan University, Ji'an 343009, China

Hyun Kyoung Yang, Jong Won Chung, Byung Kee Moon, Byung Chun Choi, and Jung Hyun Jeong[a)]
Department of Physics, Pukyong National University, Busan 608-737, Korea

Kwang Ho Kim
School of Materials Science and Engineering, Pusan National University, Busan 609-735, Korea

(Received 23 June 2011; accepted 11 October 2011)

Based on a citric acid-assisted hydrothermal method, series of Ce^{3+}/Tb^{3+} activated fluorides have been synthesized. By controlling the amount of KNO_3, the final products evolve from the Ce^{3+}/Tb^{3+} codoped orthorhombic phase GdF_3 to the Ce^{3+}/Tb^{3+} codoped cubic phase $KGdF_4$. The concentration of Ce^{3+} has great effects on the crystalline phases and the morphologies of final products. The Ce^{3+} concentration dependent samples illustrate the appearance of the hexagonal phase solid solution CeF_3–GdF_3–TbF_3 in the final products. When the Ce^{3+} concentration is 20 mol%, the sample Ce20 presents the hexagonal phase CeF_3 but the diffraction peaks move to higher degree. The x-ray diffraction patterns suggest the phase evolution of final products, the field emission scanning electron microscopy images present the variation in morphology of samples, and the photoluminescence excitation and emission spectra as well as the luminescent dynamic curves illustrate the optical properties of samples.

I. INTRODUCTION

In last few decades, rare earth compounds have been extensively studied for their practical and potential applications.[1–4] Among them, the fluorides are now receiving wide attention owing to the low-frequency phonons usually observed in their crystal lattices as well as in their thermal and environmental stabilities.[5,6] The fluoride host materials with the composition $MGdF_4$ (M = Li, Na, or K) are of particular interest.[7–11] Recently, the RE^{3+} doped KF–GdF_3 system has received more attention due to both its structural and optical properties.[12–15] In addition, Gd^{3+} is an ideal paramagnetic relaxation agent used in magnetic resonance imaging.[16,17] Therefore, the RE^{3+} doped KF–GdF_3 system is very attractive to produce single phase multifunctional materials.

Researchers have developed various synthetic strategies for the synthesis of reproducible and controllable materials. Especially, high-quality (such as monodisperse, single-crystalline, well-shaped, and phase-pure) fluorides have been fabricated successfully due to their potential applications in biology and medicine.[18–20] As a typical solution approach, the hydrothermal treatment has been proven to be effective and convenient in preparing various inorganic materials with diverse controllable morphologies and architectures.[21] In addition, the hydrothermal method is relatively simple, mild, easy, and green to produce a large amount of products; therefore, the hydrothermal route is often adopted to synthesize fluoride host materials. In the hydrothermal synthesis, there are a lot of factors to control such as reaction temperatures, reaction time, pH values of precursor solutions, reactant ratios of raw materials, and organic additives in addition to the intrinsic structures of samples. In this article, we mainly study the effects of the reactant ratios on the crystalline phases and optical properties of final products. And we select citric acid as an organic additive or surfactant in all the synthesis procedures, which can modify the morphology and the size of final products.

There have been few studies on the KF–GdF_3 system submirco/nanocrystals synthesized based on the hydrothermal method.[13,14] Moreover, the energy transfer (ET) from Ce^{3+} to Tb^{3+} has been investigated in many phosphors.[22–25] By lanthanide doping or alkaline earth doping,[26–28] the researchers have realized the phase transition in some fluorides. In this article, by controlling the amount of KNO_3, the Ce^{3+}/Tb^{3+} codoped cubic phase $KGdF_4$ samples evolve from the Ce^{3+}/Tb^{3+} codoped orthorhombic phase GdF_3. In the preparation, we find that the concentration of Ce^{3+} has great effects on the crystalline phases of the final products. The Ce^{3+} concentration dependent series of

[a)]Address all correspondence to this author.
e-mail: jhjeong@pknu.ac.kr
DOI: 10.1557/jmr.2011.388

 © Materials Research Society 2011

https://doi.org/10.1557/jmr.2011.388 Published online by Cambridge University Press

samples are also synthesized. Further, the optical properties of the final obtained products are compared and studied.

II. EXPERIMENTAL PROCEDURE

The samples were synthesized through a citric acid-assisted hydrothermal method. The raw materials Gd_2O_3 (99.9%, Sigma-Aldrich, St. Louis, MO), Tb_2O_3 (99.99%, Sigma-Aldrich, St. Louis, MO), Ce $(NO_3)_3{\cdot}6H_2O$ (99.99%, Sigma-Aldrich, St. Louis, MO), KNO_3 (99.99%, Sigma-Aldrich, St. Louis, MO), citric acid (99.5+%, Sigma-Aldrich, Tokyo, Japan), and NH_4F (≥98%, Sigma-Aldrich, Munich, Germany) were all purchased from Aldrich and used directly without further purification. The Gd $(NO_3)_3$ (0.5 M) and Tb $(NO_3)_3$ (0.02 M) stock solutions were prepared by dissolving the corresponding RE_2O_3 in nitric acid at elevated temperatures. Two millimoles of stoichiometric RE $(NO_3)_3$, 12 mmol of KNO_3, and 4 mmol of citric acid were dispersed into deionized water to form a 25 mL of clear solution by stirring. After vigorously stirred for 20 min, a 25 mL of aqueous solution containing 12 mmol of NH_4F was introduced into the solution. After stirring for another 15 min, the as-obtained solution was transferred into a 70-mL Teflon bottle held in a stainless steel autoclave, sealed, and maintained at 180 °C for 24 h. After the autoclave cooled down to room temperature naturally, the precipitates were collected by centrifugation, washed with ethanol and deionized water, and then dried in air at 60 °C for 24 h. In this article, the amounts of KNO_3 and Ce $(NO_3)_3{\cdot}6H_2O$ were adopted to study the phase transformation and the optical properties of final products. For simplicity, the 5 mol% Tb^{3+} and 10 mol% Ce^{3+} codoped samples synthesized with 0, 200, 400, and 600 mol% KNO_3 (corresponding the total amounts of RE^{3+}) are signed as K0, K200, K400, and K600, and the samples (fixed 5 mol% Tb^{3+} and 400 mol% KNO_3) synthesized with 5, 10, 20, 30, 40, 50, 70, and 95 mol% Ce^{3+} are labeled as Ce5, Ce10 (K400), Ce20, Ce30, Ce40, Ce50, Ce70, and Ce95, respectively. For comparison, the sample Ce0 was also synthesized with 400 mol% KNO_3 and without Ce^{3+}/Tb^{3+} (100 mol% Gd^{3+}) doping.

The crystalline structures of obtained samples were characterized by x-ray diffraction (XRD) patterns using a Philips X'Pert/MPD system (Eindhoven, Netherlands) with CuKα (λ = 1.54056 Å) radiation at 40 kV and 30 mA. The 2θ ranges of all the datasets are from 10 to 80° with a step size of 0.02°. Field emission scanning electron microscopy (FESEM) images were taken on a JEOL JSM-6700F (Tokyo, Japan) scanning electron microscope. The photoluminescence (PL) excitation and emission spectra were recorded using a Photon Technology International (PTI, Birmingham, NJ) fluorimeter with a xenon-arc lamp of power 60 W as excitation source. The luminescent dynamic decay curves of Tb^{3+} were measured using a phosphorimeter attachment to the PTI with a xenon-flash lamp (25 W) as excitation source. All measurements were performed at room temperature.

III. RESULTS AND DISCUSSION

A. Crystalline phase

Figure 1 shows the XRD patterns of the final products synthesized with different amounts of KNO_3 and standard data. The pattern of the sample K0 can be well indexed to the orthorhombic phase GdF_3 (space group: *Pnma* (62), JCPDS 12-0788). The sample K200 is a mixture of the orthorhombic phase GdF_3 and a new material. The diffraction peaks of the new material are denoted as *. Compared to the standard data, the new material can be indexed to the hexagonal phase CeF_3 (space group: *P*63/*mcm* (193), JCPDS 08-0045) but the positions of the diffraction peaks move toward higher degree because the ionic radius of Gd^{3+} (Tb^{3+}) is smaller than that of Ce^{3+}. According to Refs. 26–29, if the dopant concentration is over 10% in one material, this material should be called a solid solution. In the new material, the concentration of GdF_3 maybe over 10% and we believe that the new material is a solid solution of CeF_3–GdF_3–TbF_3. With the amount of KNO_3 increasing to 400 mol%, the sample K400 is a mixture of GdF_3 and $KGdF_4$. The obtained $KGdF_4$ can be readily indexed to a pure cubic phase CaF_2 (space group: *Fm*-3*m* (225), JCPDS 77-2245). As shown in the figure, the $KGdF_4$ is the main product. Pure cubic phase $KGdF_4$ is finally obtained when the amount of KNO_3 reaches 600 mol%.

The concentration of Ce^{3+} has great effects on the crystalline phases of final products. Since we want to synthesize pure cubic phase $KGdF_4$, we study the effects of the amount of Ce^{3+} on the final products using 400 mol% KNO_3 but the experimental results deviate greatly from those of expected. Figure 2 shows the Ce^{3+} concentration dependent XRD patterns of the samples synthesized with 5 mol% Tb^{3+} (except Ce0). The corresponding standard

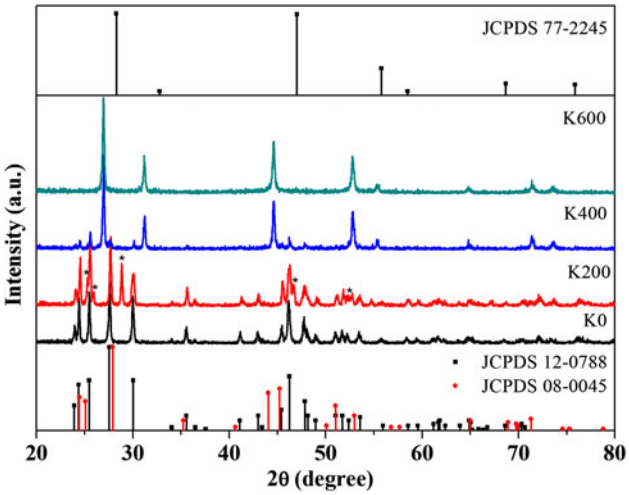


FIG. 1. X-ray diffraction (XRD) patterns of 5 mol% Tb^{3+} and 10 mol% Ce^{3+} doped samples synthesized with different amounts of KNO_3 and reference data.

https://doi.org/10.1557/jmr.2011.388 Published online by Cambridge University Press

data are listed in the figure. From the XRD pattern, it is clear that the sample Ce0 (100 mol% Gd^{3+}) is a mixture of the orthorhombic GdF_3 (JCPDS 12-0788) and the cubic phase $KGdF_4$ (JCPDS 77-2245), and the ratio of the two samples is analogous judged from the relative intensities of the diffraction peaks. When 5 mol% Ce^{3+} and 5 mol% Tb^{3+} are introduced in the raw materials, the sample Ce5 is also a mixture of $KGdF_4$ and GdF_3 but the content of GdF_3 decreases, estimated from the relative intensities of the diffraction peaks. Nearly pure $KGdF_4$ is obtained when Ce^{3+} concentration is 10 mol%. The XRD patterns of the samples Ce0, Ce5, and Ce10 illustrate that the Ce^{3+}/Tb^{3+} doping contributes to the formation of $KGdF_4$. When the Ce^{3+} concentration increases to 20 mol%, the XRD pattern of the sample Ce20 can be indexed to the hexagonal phase CeF_3 (JCPDS 08-0045) and the diffraction peaks move to higher degree because the ion radius of Gd^{3+} (Tb^{3+}) is smaller than that of Ce^{3+}. The sample should be a solid solution of CeF_3–GdF_3–TbF_3. Though the concentration of Ce^{3+} is only 20 mol%, the sample presents the hexagonal phase of CeF_3. With the increase of the Ce^{3+} concentration, the samples can also be indexed to CeF_3, the relative diffraction intensities change and become weaker, and the diffraction peaks move to lower degree as well. The XRD evolution of the sample synthesized with different Ce^{3+} concentration proves the existence of the solid solution of CeF_3–GdF_3–TbF_3 in the final products.

B. Morphology

The FESEM images of the samples synthesized with different amounts of KNO_3 are illustrated in Fig. 3. The GdF_3 [sample K0; Fig. 3(a)] sample has a cookie-like morphology with a hole in the center which is aggregate of several particles with an average size of 100 nm. The sample K200 [Fig. 3(b)] displays various morphologies: diamond shape (GdF_3), hexagonal disks (solid solution of CeF_3–GdF_3–TbF_3), and some particles (GdF_3). Figure 3(c) is the FESEM image of the sample K400, which has spherical morphology with an average diameter of 130 nm. The inset in Fig. 3(c) is a single spherical particle. By increasing the content of KNO_3 to 600 mol%, the sample K600 attains spherical morphology and the size of the spherical particles becomes larger in an average diameter which is 150 nm as shown in Fig. 3(d). A single particle in the inset of Fig. 3(d) illustrates that.

Figure 4 presents the FESEM images of the Ce^{3+} concentration dependent samples. The sample Ce5 [mixture of $KGdF_4$ and GdF_3; Fig. 4(a)] is also diamond shaped (GdF_3) and has spherical ($KGdF_4$) morphology. The sample Ce10 (K400) has spherical morphology as illustrated in Fig. 3(c). Great change happens with the sample Ce20, which is a solid solution of hexagonal phase CeF_3–GdF_3–TbF_3. The sample presents hexagonal disk morphology with an average size of 200 nm in edge length and 20 nm in breadth as shown in Fig. 4(b). When the concentration of Ce^{3+} increases to 50 mol% [Fig. 4(c)], the sample Ce50 is composed of spherical-like particles with an average size of 50 nm. The 5 mol% Tb^{3+} doped CeF_3 (Ce95) nanocrystals in Fig. 4(d) are smaller particles (about 30 nm) than those in Fig. 4(c). The FESEM images agree well with the XRD data.

As shown in Figs. 3 and 4, the concentrations of KNO_3 and Ce^{3+} also have great effects on the morphology of final products. The morphology has great relations with the synthesis conditions and methods in addition to the intrinsic structural properties of the samples. In our experiment, when no KNO_3 was added in the raw material, the GdF_3 [sample K0; Fig. 3(a)] was cookie-like with a hole in the center. When 200 mol% KNO_3 was added in the raw material, the GdF_3 was diamond shaped. The sample K400, which was made of GdF_3 and $KGdF_4$, was spherical with an average diameter of 130 nm. The experimental results suggest that the concentration of K^+ has great effects on the morphology of the GdF_3. The formation mechanism of the morphology has a lot of work to do with the pH values of the prepared solutions, the concentration of ions in the solutions, and so on, which will be studied in the future.

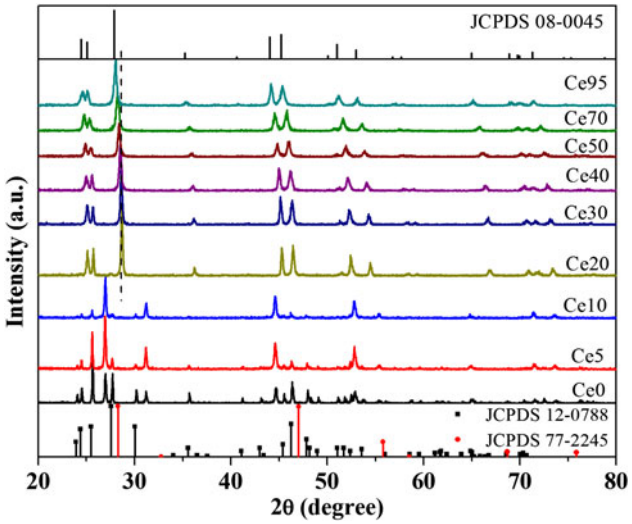


FIG. 2. XRD patterns of final products dependence on Ce^{3+} concentration and standard data.

C. Possible phase transition mechanism

Based on the analysis of XRD results and the FESEM images, we speculate one possible mechanism for the phase transition of final products. For the KNO_3 concentration dependent samples, when no KNO_3 was added in the raw materials, the final product was GdF_3. When 200 mol% KNO_3 was introduced, the hexagonal phase solid solution of CeF_3–GdF_3–TbF_3 emerged beside GdF_3. We believed that the emergence of KNO_3 affected the

https://doi.org/10.1557/jmr.2011.388 Published online by Cambridge University Press

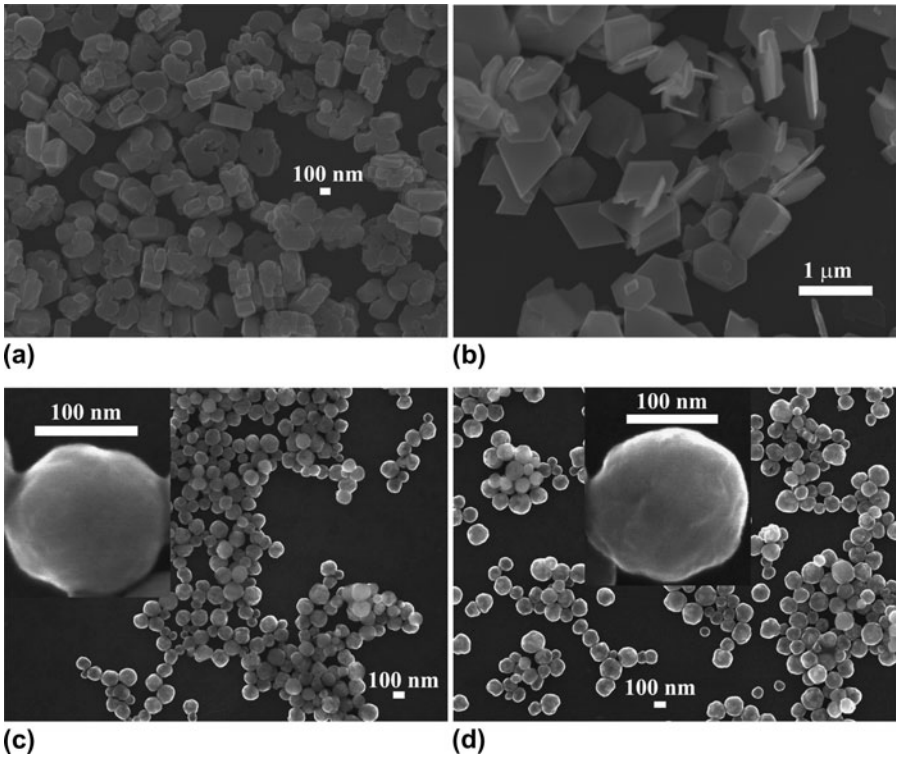


FIG. 3. Field emission scanning electron microscopy (FESEM) images of final products (a) K0, (b) K200, (c) K400, and (d) K600. Insets in Figs. 3(c) and 3(d) are single spherical particles of corresponding samples.

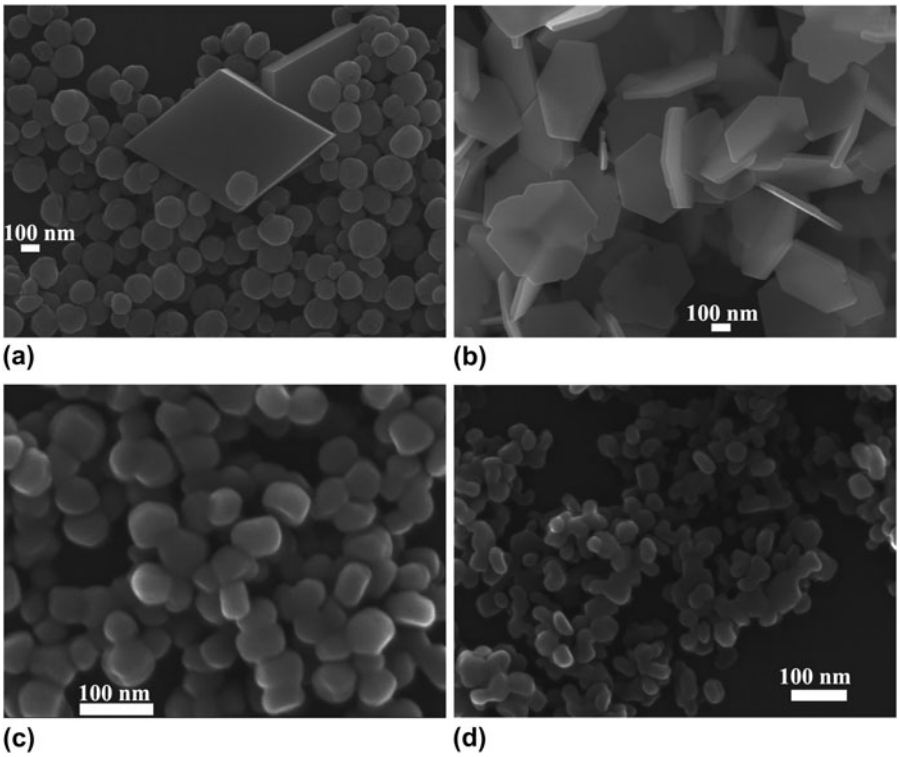


FIG. 4. FESEM images of samples (a) Ce5, (b) Ce20, (c) Ce50, and (d) Ce95.

https://doi.org/10.1557/jmr.2011.388 Published online by Cambridge University Press

reaction between F^- and RE^{3+}, but it did not participate in the chemical reaction because there was no potassium compound in the sample K200. Since the basicity of the RE_2O_3 along the rare earth series gradually decreases, the CeF_3 was easier to be formed than that of GdF_3 so the solid solution of CeF_3–GdF_3–TbF_3 was formed simultaneously. When the concentration of KNO_3 increased to 400 or 600 mol%, K^+ participated in the reactant reaction and the $KGdF_4$ was formed. For the Ce^{3+} concentration dependent samples, KNO_3 was fixed as 400 mol%. The CeF_3 was easier to be formed than the GdF_3. When the concentration of Ce^{3+} was only 20 mol%, the sample presented the hexagonal phase indicating the high capacity of CeF_3, which meant that the final product presented the CeF_3 phase though the concentration of CeF_3 was low. For simplicity, the proposed possible phase transition mechanism of the samples based on the present data is illustrated in Scheme 1. There is a lot of work to do to analyze the mechanism of the phase transition, which we purport in the future.

D. Optical properties

Figure 5 shows the PL excitation spectra of the samples synthesized with different amounts of KNO_3. By monitoring at 544-nm emission of the Tb^{3+}, the sample GdF_3 (K0) presents a broad excitation band peaking at 260 nm, which can be attributed to the electric dipole-allowed 4f → 5d transition of Ce^{3+}.[30] In addition, there are excitation peaks at around 274 and 312 (307) nm which can be assigned to the $^8S_{7/2} \rightarrow {}^6I_J$ and $^8S_{7/2} \rightarrow {}^6P_J$ transitions of host Gd^{3+}, respectively.[30] The presence of Gd^{3+} excitation peaks in the PL excitation spectra indicates the existence of ET from Gd^{3+} to Tb^{3+}. In the wavelength range of 320–400 nm, there are weak characteristic transitions of forbidden 4f → 4f transitions within the Tb^{3+} configuration.[22,24] A shoulder at about 285 nm emerges in the sample K200 beside the main band peaking at 261 nm. The excitation spectra of both the samples K400 and K600 have only one main band peaking at about 293 nm. The disappearance of excitation band at 261 nm (260 nm) suggests the variations of the located lattices of Ce^{3+}, which prove the phase evolution of the final products. The variation of the excitation spectra of sample agrees well with the XRD data. The final products change from the Ce^{3+}/Tb^{3+} codoped orthorhombic phase GdF_3, to a mixture of the orthorhombic phase GdF_3 and the hexagonal phase solid solution of CeF_3–GdF_3–TbF_3 and to the pure cubic phase $KGdF_4$ finally; the 4f → 5d band of Ce^{3+} is sensitive to the host environment so the

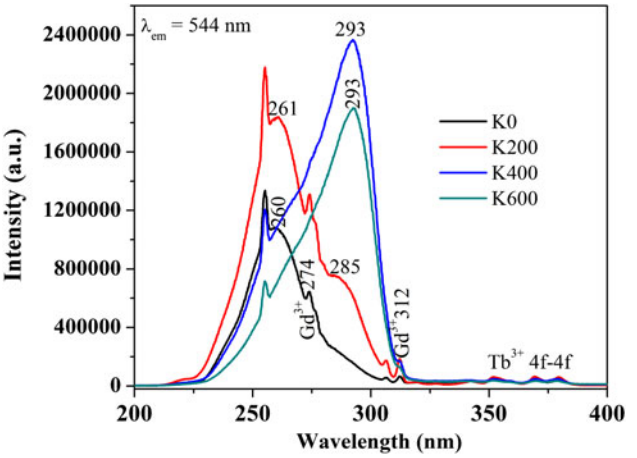


FIG. 5. Photoluminescence (PL) excitation spectra of Ce^{3+}/Tb^{3+} doped final products synthesized with different amounts of KNO_3.

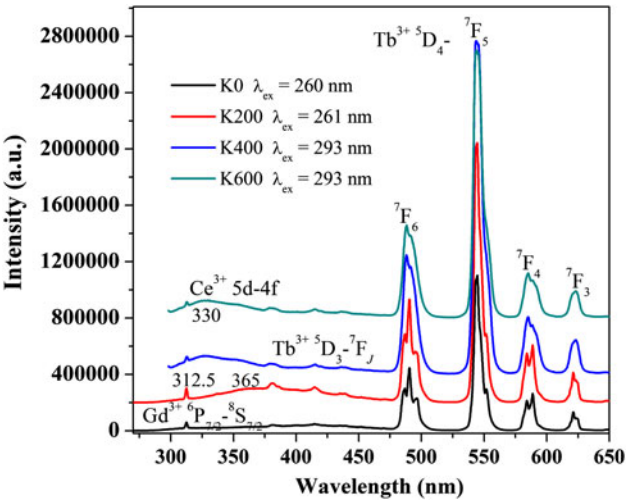
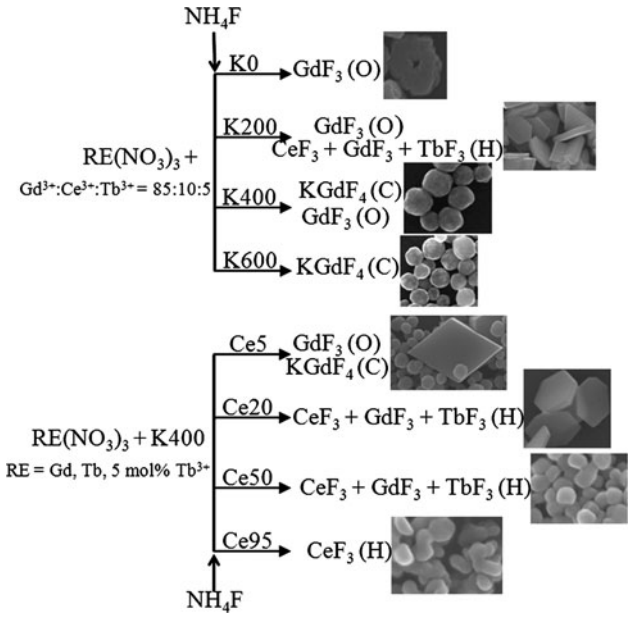


FIG. 6. PL emission spectra of Ce^{3+}/Tb^{3+} doped final products synthesized with different amounts of KNO_3.



SCHEME 1. Possible phase transition mechanism of the samples. Online TOC

https://doi.org/10.1557/jmr.2011.388 Published online by Cambridge University Press

excitation bands of Ce^{3+} in the final products change, which prove the phase evolution of the final products.

The PL excitation spectra change with the amount of KNO_3; correspondingly, the PL emission spectra will also change because the 5d → 4f transition of Ce^{3+} and the 4f → 4f transitions of Tb^{3+} are both sensitive to the environment of the local lattices. With Ce^{3+} sensitization, the PL emission spectra of samples K0, K200, K400, and K600 are illustrated in Fig. 6. The characteristic emission of Tb^{3+} $^5D_4 \rightarrow {}^7F_6$, $^5D_4 \rightarrow {}^7F_5$, $^5D_4 \rightarrow {}^7F_4$, and $^5D_4 \rightarrow {}^7F_3$ transitions are observed.[22,24,30] As shown in the figure, the splits of Tb^{3+} emissions of the samples become inconspicuous with the increase of the amount of KNO_3 (phase evolution). The emission bands of Ce^{3+} 5d → 4f are very different in the final products. Ce^{3+} has nearly no emission in the sample K0; it has a broad emission band peaking at about 365 nm in the sample K200; and the emission bands shift to about 330 nm in the samples K400 and K600, respectively. In addition, there are emissions of Gd^{3+} $^6P_{7/2} \rightarrow {}^8S_{7/2}$ peaking at 312.5 nm in the spectra, which indicate the existence of ET from Ce^{3+} to Gd^{3+}.[30] As shown in the figure, the emission intensities of Gd^{3+} are also different in the samples.

By monitoring at 544-nm emission of the Tb^{3+}, the PL excitation spectra dependence on the Ce^{3+} concentration are illustrated in Fig. 7. According to the main peak positions and the spectral profiles, the excitation spectra can be divided into three groups: the first group including the samples Ce5 and Ce10, the main excitation peaks locate at 293 nm though there are shoulders at about 265 and 274 nm; the second group including the samples Ce20, Ce30, Ce40, Ce50, and Ce70, the spectra only have one main peak and the peak position is red shifted from 261, 264, 267, 269, to 270 nm with the increase of Ce^{3+} concentration; and the third group including Tb^{3+} doped CeF_3 (Ce95), which has one main peak positioned at about 263 nm.

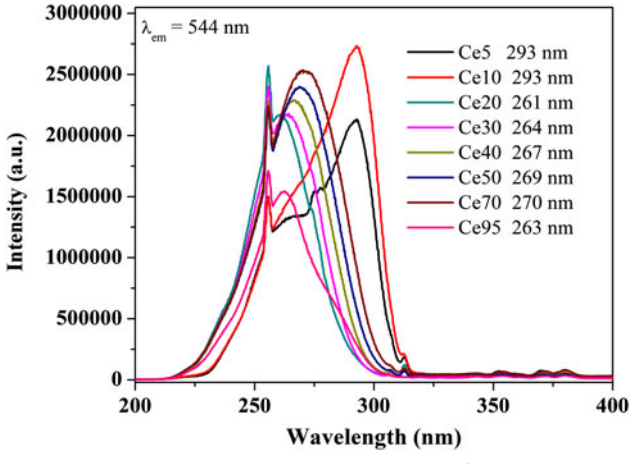


FIG. 7. PL excitation spectra dependence on Ce^{3+} concentration.

Correspondingly, the PL emission spectra can also be divided into three groups. Figure 8 shows the PL emission spectra dependent on the Ce^{3+} concentration. In the first group (samples Ce5 and Ce10), not only the emission of Tb^{3+} but also the emission of Ce^{3+} become stronger with the increase of Ce^{3+} concentration. In the second group, the Ce^{3+} concentration is in the range of 20–70 mol% and the samples are in hexagonal phase. The Ce^{3+} has nearly no emissions compared to those in the first group. The emissions of Tb^{3+} increase slightly with the concentration increase of Ce^{3+} and the spectral profiles become smooth. In the third group (the sample Ce95, 5 mol% Tb^{3+} doped CeF_3), the emission of Gd^{3+} disappears as there is no Gd^{3+} in the sample and the emissions of Tb^{3+} become weaker compared to the other samples.

Based on previous studies of ETs in Ce^{3+}/Tb^{3+} codoped gadolinium compounds[30,31] and the above PL excitation and emission spectra, we believe that the excitation energy

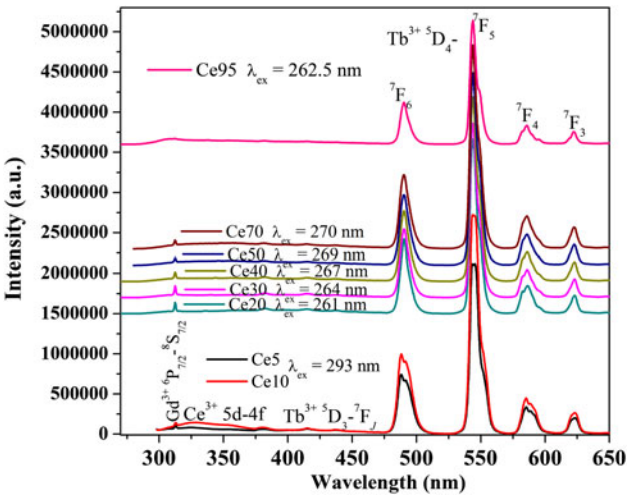


FIG. 8. PL emission spectra dependence on Ce^{3+} concentration.

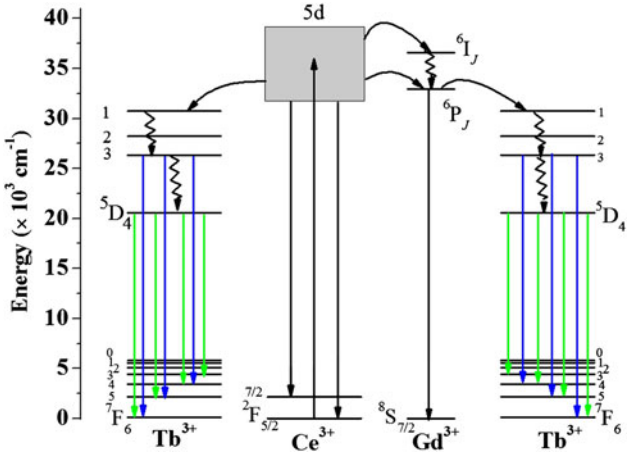


FIG. 9. Schematic energy level diagrams of Ce^{3+}, Tb^{3+}, Gd^{3+}, and possible excitation and emission processes.

https://doi.org/10.1557/jmr.2011.388 Published online by Cambridge University Press

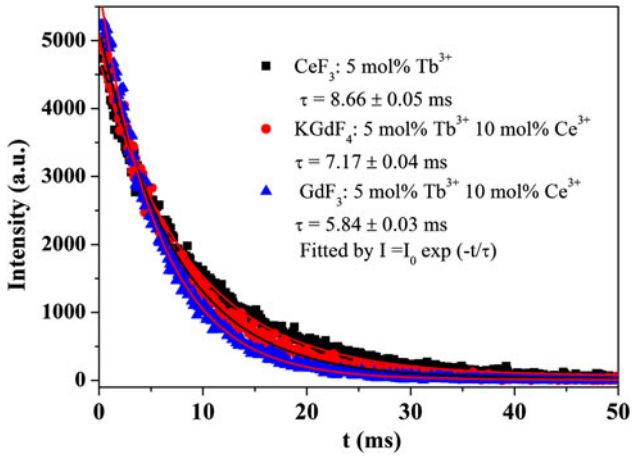


FIG. 10. Decay curves of Tb^{3+} $^5D_4 \rightarrow {}^7F_5$ in representative samples.

TABLE I. Spectroscopic parameters for $^5D_4 \rightarrow {}^7F_5$ lifetimes of Tb^{3+}.

Sample	λ_{ex} (nm)	τ (ms)	Sample	λ_{ex} (nm)	τ (ms)
K0	260	5.84 ± 0.03	Ce20	261	8.71 ± 0.04
K200	261	5.63 ± 0.02	Ce30	265	9.10 ± 0.06
K400	293	7.53 ± 0.04	Ce40	267.5	9.33 ± 0.06
K600	293	7.17 ± 0.04	Ce50	270	8.74 ± 0.05
Ce5	261	6.49 ± 0.03	Ce70	270	9.01 ± 0.05
293	7.51 ± 0.04	Ce95	261	8.66 ± 0.05	

is absorbed by Ce^{3+} 4f → 5d transition and then mainly transferred to Tb^{3+} in $KGdF_4$, where the energy is released as visible emissions. In addition, Ce^{3+} can transfer energy to Gd^{3+} and then Gd^{3+} transfers the energy to Tb^{3+}. In the GdF_3 and the solid solution of CeF_3–GdF_3–TbF_3, the excitation energy is absorbed by Ce^{3+} 4f → 5d transition and then mainly transferred to Gd^{3+} as the energy levels match well and then Gd^{3+} transfers the energy to Tb^{3+}. And in CeF_3, the excitation energy is absorbed by Ce^{3+} 4f → 5d transition and then transferred to Tb^{3+} directly. Figure 9 is schematic energy level diagram of Ce^{3+}, Tb^{3+}, and Gd^{3+}, and possible excitation and emission processes are plotted in this figure. It illustrates that the luminescent process starts with excitation of Ce^{3+} followed by ET process from Ce^{3+} to Tb^{3+} directly or to Gd^{3+} to Tb^{3+}, and then the energy is released by them. From the PL spectra of the samples, we can infer that the excitation energy can be released by Ce^{3+} before ET occurs from Ce^{3+} to Tb^{3+} (Gd^{3+}) or by Gd^{3+} in the energy migration among host lattices.

Figure 10 is the luminescent decay curves monitoring at the $^5D_4 \rightarrow {}^7F_5$ transition of Tb^{3+} in the representative samples Ce95, K600, and K0. The decay curves can be well fitted by a single exponential function $I(t) = I_0 \exp(-t/\tau)$, where I_0 is the initial emission intensity at $t = 0$ and τ is the 1/e lifetime of Tb^{3+}. The τ (8.66 ± 0.05 ms) in the hexagonal CeF_3 (Ce95) is longer than that in the cubic phase $KGdF_4$ (K600, 7.17 ± 0.04 ms) or the orthorhombic phase GdF_3 (K0, 5.84 ± 0.03 ms). The measurement conditions and deduced lifetimes of Tb^{3+} in all the samples are listed in Table I.

IV. CONCLUSIONS

In conclusion, by controlling the amount of KNO_3, the final products evolve from the orthorhombic phase GdF_3, to a mixture of the orthorhombic phase GdF_3 and the hexagonal phase solid solution of CeF_3–GdF_3–TbF_3 and finally to the cubic phase $KGdF_4$. The Ce^{3+} concentration dependent final products prove the existence of the hexagonal phase solid solution CeF_3–GdF_3–TbF_3. The XRD patterns and the FESEM images illustrate the phase transformation and the variation in morphology of the samples. Since Ce^{3+} is sensitive to the local symmetry, Ce^{3+} presents different optical properties in sensitizing Tb^{3+} emission in the samples as well as its own emissions. Tb^{3+} also presents different emissions in the final products because its 4f → 4f transition is affected by the local symmetry around Tb^{3+}. The PL spectra and the luminescent dynamic curves clearly demonstrate the variations in optical properties of the samples.

ACKNOWLEDGMENTS

This research was supported by Basic Science Research Program through the National Research Foundation of Korea (NRF) funded by the Ministry of Education, Science and Technology (No. 2010-0022540) and this research was also supported by NCRC (National Core Research Center) program through the NRF funded by the Ministry of Education, Science and Technology (No. 2010-0001-226).

REFERENCES

1. F. Wang and X.G. Liu: Recent advances in the chemistry of lanthanide-doped upconversion nanocrystals. *Chem. Soc. Rev.* **38**, 976 (2009).
2. S.V. Eliseeva and J.C. Bünzli: Lanthanide luminescence for functional materials and bio-sciences. *Chem. Soc. Rev.* **39**, 189 (2010).
3. B. Yan and J.H. Wu: Facile composite synthesis and photoluminescence of $NaGd(MoO_4)_2$: Ln^{3+} (Ln = Eu, Tb) submicrometer phosphors. *J. Mater. Res.* **24**, 32 (2009).
4. C-H. Liang, Y-C. Chang, Y-S. Chang, and S. Wu: Photoluminescence properties of Eu^{3+}-doped BaY_2ZnO_5 phosphors under near-ultraviolet irradiation. *J. Mater. Res.* **25**, 850 (2010).
5. C.X. Li and J. Lin: Rare earth fluoride nano-/microcrystals: Synthesis, surface modification and application. *J. Mater. Chem.* **20**, 6831 (2010).
6. P.R. Diamente, M. Raudsepp, and F.C.J.M. van Veggel: Dispersible Tm^{3+}-doped nanoparticles that exhibit strong 1.47 μm photoluminescence. *Adv. Funct. Mater.* **17**, 363 (2007).
7. R.T. Wegh, H. Donker, K.D. Oskam, and A. Meijerink: Visible quantum cutting in $LiGdF_4$:Eu^{3+} through downconversion. *Science* **283**, 663 (1999).

https://doi.org/10.1557/jmr.2011.388 Published online by Cambridge University Press

8. F.T. You, S.H. Huang, S.M. Liu, and Y. Tao: VUV excited luminescence of $MGdF_4:Eu^{3+}$ (M=Na, K, NH_4). *J. Lumin.* **110**, 95 (2004).
9. P. Ptacek, H. Schäfer, K. Kömpe, and M. Haase: Crystal phase control of luminescing α-$NaGdF_4:Eu^{3+}$and β-$NaGdF_4:Eu^{3+}$ nanocrystals. *Adv. Funct. Mater.* **17**, 3843 (2007).
10. X.H. Liu, L.M. Wang, Z.Y. Wang, and Z.Q. Li: Synthesis of biocompatible and luminescent $NaGdF_4$:Yb,Er@carbon nanoparticles in water-in-oil microemulsion. *J. Mater. Res.* **26**, 82 (2011).
11. F. He, P.P. Yang, D. Wang, N. Niu, S.L. Gai, and X.B. Li: Self-assembled β-$NaGdF_4$ microcrystals: Hydrothermal synthesis, morphology evolution, and luminescence properties. *Inorg. Chem.* **50**, 4116 (2011).
12. T. Lee, L. Luo, W. Diau, T. Chen, B. Cheng, and C. Tung: Visible quantum cutting through downconversion in green-emitting $K_2GdF_5:Tb^{3+}$ phosphors. *Appl. Phys. Lett.* **89**, 131121 (2006).
13. L.W. Yang, Y.Y. Zhang, J.J. Li, Y. Li, J.X. Zhong, and P.K. Chu: Magnetic and upconverted luminescent properties of multifunctional lanthanide doped cubic $KGdF_4$ nanocrystals. *Nanoscale* **2**, 2805 (2010).
14. C.Y. Cao, H.K. Yang, J.W. Chung, B.K. Moon, B.C. Choi, J.H. Jeong, and K.H. Kim: Hydrothermal synthesis and enhanced photoluminescence of Tb^{3+} in Ce^{3+}/Tb^{3+} doped $KGdF_4$ nanocrystals. *J. Mater. Chem.* **21**, 10342 (2011).
15. Y-P. Du, Y-W. Zhang, L-D. Sun, and C-H. Yan: Optically active uniform potassium and lithium rare earth fluoride nanocrystals derived from metal trifluroacetate precursors. *Dalton Trans.* 8574 (2009).
16. R. Kumar, M. Nyk, T. Ohulchanskyy, C. Flask, and P. Prasad: Combined optical and MR bioimaging using rare earth ion doped $NaYF_4$ nanocrystals. *Adv. Funct. Mater.* **19**, 853 (2009).
17. Y. Park, J. Kim, K. Lee, K. Jeon, H. Na, J. Yu, H. Kim, N. Lee, S. Choi, S. Baik, H. Kim, S. Park, B. Park, Y. Kim, S. Lee, S. Yoon, I. Song, W. Moom, Y. Suh, and T. Hyeon: Nonblinking and nonbleaching upconverting nanoparticles as an optical imaging nanoprobe and T1 magnetic resonance imaging contrast agent. *Adv. Mater.* **21**, 4467 (2009).
18. Karvianto and G.M. Chow: The effects of surface and surface coatings on fluorescence properties of hollow $NaYF_4$:Yb,Er upconversion nanoparticles. *J. Mater. Res.* **26**, 70 (2011).
19. L.P. Qian, D. Yuan, G.S. Yi, and G.M. Chow: Critical shell thickness and emission enhancement of $NaYF_4$:Yb,Er/$NaYF_4$/silica core/shell/shell nanoparticles. *J. Mater. Res.* **24**, 3559 (2009).
20. G.F. Wang and Q. Peng: Synthesis and tunable photoluminescence of $NaYF_4$:Eu/Ba nanocrystals. *J. Mater. Res.* **25**, 2422 (2010).
21. J.H. Liang, Q. Peng, X. Wang, X. Zheng, R.J. Wang, X.P. Qiu, C.W. Nan, and Y.D. Li: Chromate nanorods/nanobelts: General synthesis, characterization, and properties. *Inorg. Chem.* **44**, 9405 (2005).
22. Y.J. Huang, H.P. You, G. Jia, Y.H. Song, Y.H. Zheng, M. Yang, K. Liu, and N. Guo: Hydrothermal synthesis, cubic structure, and luminescence properties of $BaYF_5$:RE (RE = Eu, Ce, Tb) nanocrystals. *J. Phys. Chem. C* **114**, 18051 (2010).
23. G.G. Zhang, J. Wang, Y. Chen, and Q. Su: Two-color emitting of Ce^{3+} and Tb^{3+} co-doped $CaLaGa_3S_6O$ for UV LEDs. *Opt. Lett.* **35**, 2382 (2010).
24. Y.Q. Lei, M. Pang, W.Q. Fan, J. Feng, S.Y. Song, S. Dang, and H.J. Zhang: Microwave-assisted synthesis of hydrophilic $BaYF_5$: Tb/Ce,Tb green fluorescent colloid nanocrystals. *Dalton Trans.* **40**, 142 (2011).
25. H. Guo, H. Zhang, J.J. Li, and F. Li: Blue-white-green tunable luminescence from $Ba_2Gd_2Si_4O_{13}:Ce^{3+},Tb^{3+}$ phosphors excited by ultraviolet light. *Opt. Express* **18**, 27257 (2010).
26. F. Wang, Y. Han, C.S. Lim, Y.H. Lu, J. Wang, J. Xu, H.Y. Chen, C. Zhang, M.H. Hong, and X.G. Liu: Simultaneous phase and size control of upconversion nanocrystals through lanthanide doping. *Nature* **463**, 1061 (2010).
27. D.Q. Chen, Y.L. Yu, F. Huang, A.P. Yang, and Y.S. Wang: Lanthanide activator doped $NaYb_{1-x}Gd_xF_4$ nanocrystals with tunable down-, up-conversion luminescence and paramagnetic properties. *J. Mater. Chem.* **21**, 6186 (2011).
28. D.Q. Chen, Y.L. Yu, F. Huang, and Y.S. Wang: Phase transition from hexagonal LnF_3 (Ln = La, Ce, Pr) to cubic $Ln_{0.8}M_{0.2}F_{2.8}$ (M = Ca, Sr, Ba) nanocrystals with enhanced upconversion induced by alkaline-earth doping. *Chem. Commun.* **47**, 2601 (2011).
29. D.Q. Chen, Y.L. Yu, F. Huang, P. Huang, A.P. Yang, and Y.S. Wang: Modifying the size and shape of monodisperse bifunctional alkaline-earth fluoride nanocrystals through lanthanide doping. *J. Am. Chem. Soc.* **132**, 9976 (2010).
30. C.X. Li, P.A. Ma, P.P. Yang, Z.H. Xu, G.G. Li, D.M. Yang, C. Peng, and J. Lin: Fine structural and morphological control of rare earth fluorides REF_3 (RE = La–Lu, Y) nano/microcrystals: Microwave-assisted ionic liquid synthesis, magnetic and luminescent properties. *CrystEngComm* **13**, 1003 (2011).
31. G. Blasse: The physics of new luminescent materials. *Mater. Chem. Phys.* **16**, 201 (1987).

https://doi.org/10.1557/jmr.2011.388 Published online by Cambridge University Press